



# Optical Flux and Spectral Variability of BL Lacertae during Its Historical High Outburst in 2020

Nibedita Kalita<sup>1,2,10</sup> , Yuhai Yuan<sup>3,4</sup> , Minfeng Gu<sup>1</sup> , Junhui Fan<sup>3,4</sup> , Yosuke Mizuno<sup>5,6</sup> , Peng Jiang<sup>2</sup>, Alok C. Gupta<sup>1,7</sup> , Hongyan Zhou<sup>2</sup>, Xiang Pan<sup>2</sup> , Anton A. Strigachev<sup>8</sup>, Rumen S. Bachev<sup>8</sup> , and Lang Cui<sup>9</sup>

<sup>1</sup> Key Laboratory for Research in Galaxies and Cosmology, Shanghai Astronomical Observatory, Chinese Academy of Sciences, 80 Nandan Road, Shanghai 200030, People's Republic of China; [nibeditakt1@gmail.com](mailto:nibeditakt1@gmail.com)

<sup>2</sup> Key Laboratory for Polar Science, MNR, Polar Research Institute of China, 451 Jinqiao Road, Shanghai 200135, People's Republic of China

<sup>3</sup> Center for Astrophysics, Guangzhou University, Guangzhou 510006, People's Republic of China

<sup>4</sup> Astronomy Science and Technology Research Laboratory, Department of Education of Guangdong Province, Guangzhou 510006, People's Republic of China

<sup>5</sup> Tsung-Dao Lee Institute, Shanghai Jiao Tong University, 520 Shengrong Road, Shanghai, 201210, People's Republic of China

<sup>6</sup> School of Physics and Astronomy, Shanghai Jiao Tong University, 800 Dongchuan Road, Shanghai, 200240, People's Republic of China

<sup>7</sup> Aryabhata Research Institute of Observational Sciences (ARIES), Manora Peak, Nainital, 263001, India

<sup>8</sup> Institute of Astronomy and National Astronomical Observatory, Bulgarian Academy of Sciences, 72 Tsarigradsko shosse Boulevard, 1784 Sofia, Bulgaria

<sup>9</sup> Xinjiang Astronomical Observatory, Chinese Academy of Sciences, 150 Science 1-Street, 830011 Urumqi, People's Republic of China

Received 2022 August 30; revised 2022 November 24; accepted 2022 November 30; published 2023 February 2

## Abstract

BL Lacertae underwent a series of historical high flux activity over a year from 2020 August in the optical to VHE  $\gamma$ -rays. In this paper, we report on optical flux and spectral variability of the first historical maxima outburst event during October–November in the  $g$ ,  $r$ , and  $i$  bands with the 1.26 m telescope at the Xinglong Observatory, China. We detected significant intranight variations with amplitude rising up to  $\sim 30\%$ , where the fastest variability timescale was found to be a few tens of minutes, giving an emitting region size of the order  $10^{-3}$  pc, which corresponds to  $\sim 100$  Schwarzschild radius of the central black hole, likely coming from some jet mini-structures. Unlike on the intranight timescale, a clear frequency-dependent pattern along symmetric timescales ( $\sim 11$  days) of flux variation is detected on a long timescale. The spectral evolution was predominated by flattening of the spectra with increasing brightness i.e., a bluer-when-brighter trend in 96% of the cases. On the night before the outburst peak, the color indices shown in a color–magnitude diagram, clustered into two distinct branches, within a period of  $\sim 6$  hr, which is connected to a hard-soft-hard spectral evolution trend extracted from time-resolved spectra. To the best of our knowledge, such a trend has never been seen in BL Lac or any other blazars before. The results obtained in this study can be explained in the context of shock-induced particle acceleration or magnetic reconnection in the jet where turbulent processes most likely resulted in the asymmetric flux variation on a nightly timescale.

*Unified Astronomy Thesaurus concepts:* Active galactic nuclei (16); Blazars (164)

## 1. Introduction

BL Lacertae is the prototype of BL Lac objects that belong to the most energetic radio-loud class of active galactic nuclei (AGNs) known as blazars. The source is hosted by an elliptical galaxy of brightness  $R = 15.5$  located at a redshift of  $z = 0.0668$  in the northern hemisphere. Based on the location of synchrotron peak frequency in the spectral energy distribution (SED), it is classified as either an LBL (low synchrotron peaked) or IBL (intermediate synchrotron peaked) blazar as it has been found to shift its peak energy on different occasions (Ackermann et al. 2011; Fan et al. 2016; Nilsson et al. 2018). The source has been detected in teraelectronvolt energies (Neshpor et al. 2001; Albert et al. 2007) and found to show rapid flux variation within a few minutes in the  $\gamma$ -rays during high-activity states, which coincides with the emergence of a new superluminal component from the radio core accompanied by changes in the optical polarization angle (Arlen et al. 2013).

BL Lacertae (hereafter BL Lac) is one of the most frequently and well-studied blazar in the multiwavelength domain. This blazar has been a target of numerous multiwavelength observation campaigns (e.g., Hagen-Thorn et al. 2002; Böttcher et al. 2003; Villata et al. 2004; Bach et al. 2006; Raiteri et al. 2009, 2010; MAGIC Collaboration et al. 2019). The broadband spectrum of the source could be interpreted via either a single-zone or a two-zone SSC model; however, an EC component +SSC model is the most likely explanation for the observed variability in the source (Abdo et al. 2011; Sahakyan & Giommi 2022). The optical spectra of the source show the presence of both broad and narrow emission lines during a not unusually faint state when the continuum polarization was estimated as being relatively low (Corbett et al. 1996). The study found that the  $H_\alpha$  emission could be powered by thermal radiation from an accretion disk without significantly affecting the shape or polarization of the optical continuum. Later, Capetti et al. (2010) found that the flux variation in  $H_\alpha$  and  $H_\beta$  emission lines resulted from the addition of gas in the broad line region (BLR).

A study carried out by Marscher et al. (2008) found that a bright feature in the jet causes a multiwavelength double flare originating in the acceleration and collimation zone in a helical magnetic field. The existence of a helical magnetic field in BL Lac resulted in the observed alternation of enhanced and

<sup>10</sup> Asian Forum for Polar Sciences Fellow.

**Table 1**  
CSs of BL Lac

CSs (1)	$m_V \pm \sigma_V$ (2)	$m_R \pm \sigma_R$ (3)	$m_I \pm \sigma_I$ (4)	$m_g$ (5)	$m_r$ (6)	$m_i$ (7)
B	12.78 $\pm$ 0.04	11.93 $\pm$ 0.05	11.09 $\pm$ 0.06	13.67	12.01	11.17
C	14.19 $\pm$ 0.03	13.69 $\pm$ 0.03	13.23 $\pm$ 0.04	14.76	13.74	13.27

**Note.** Column (1): the standard stars of BL Lac are labeled B and C; Columns (2)–(4): magnitudes with the standard deviation at the  $V$ ,  $R$ , and  $I$  bands, respectively, and Columns (5)–(7): magnitudes at the  $g$ ,  $r$ , and  $i$  bands, respectively.

suppressed optical activity that was accompanied by hard and soft radio events, respectively (Villata et al. 2009; Cohen et al. 2015). Evidence of multiple standing shocks along with helical magnetic fields was also reported from polarimetric space very long baseline interferometry observations by RadioAstron (Gómez et al. 2016).

Variation in the blazar flux over a timescale of a few minutes to less than a day is commonly known as intraday variability (IDV; Wagner & Witzel 1995), while variability timescales of weeks to a few months and months to years are known as short-term variability (STV) and long-term variability (LTV), respectively (Gupta et al. 2004). BL Lac is well known for its optical flux and polarization variability on diverse timescales, and hence, has been observed by several observatories on different occasions and studies have been carried out to understand the physical properties (Massaro et al. 1998; Raiteri et al. 2013; Gaur et al. 2015; Weaver et al. 2020). Weaver et al. (2020) reported that turbulent plasma is responsible for multiwavelength timescales of variability, lags in cross-frequency variation, and polarization properties where shock in the jet energizes the plasma, which subsequently loses energy via synchrotron and inverse Compton radiation in a strong B field of strength  $\sim 3$ G. It has been found to show anticorrelated flux and polarization where PA was almost non-variable (Gaur et al. 2014). On several occasions, microvariations have been detected in the source accompanied by flattening of the spectra with increasing brightness popularly known as the bluer-when-brighter (BWB) trend (Miller et al. 1989; Papadakis et al. 2003; Gu et al. 2006; Agarwal & Gupta 2015; Bhatta & Webb 2018). Such microvariations could have resulted from perturbations of different regions in the jet that cause localized injections of relativistic particles on timescales much shorter than the average sampling interval of the light curves where the cooling and light-crossing timescales control the variations (Papadakis et al. 2003). The lag between spectral and flux changes detected in a long-term study by Papadakis et al. (2007) made with WEBT observations was explained in terms of Doppler factor variations due to changes in the viewing angle of a curved and inhomogeneous emitting jet.

Recently, the source has undergone prolonged episodes of historical high flux activity starting from 2020 August until 2021 August, in the optical to VHE  $\gamma$ -rays ( $>100$  GeV) (ATel# 13930, Grishina & Larionov 2020; ATel# 13933, Cheung 2020; ATel# 13963, Blanch 2020; ATel# 13964, Ojha & Valverd 2020). In the optical, the source reached its first historical high flux state on 2020 October 5 with a recorded  $R$ -band magnitude of  $11.73 \pm 0.01$  observed by the Kanata telescope (ATel# 14081, Sasada et al. 2020). After the first flare, the source attained an even brighter phase with magnitudes below  $R = 11.5$  recorded by the WEBT Collaboration on 2021 January 17 (ATel# 14342, D’Ammando 2021), and on July 31, it reached the brightest state ever by going down to  $11.271 \pm 0.003$  mag (ATel# 14820, Kunkel et al. 2021).

Following the astronomer’s telegram on the first enhanced activity of the source in 2020, we monitored the source starting from 2020 October 1 to November 23 in the  $g$ ,  $r$ , and  $i$  filter bands with a 1.26 m telescope located at the Xinglong Observatory in China. We recorded the first optical flare along with its rising and decaying phase during the series of high-activity events. In this paper, we have investigated the temporal and spectral behaviors of the blazar in the optical band and are presenting our first result. This paper is structured as follows. In Section 2, we describe our photometric observations and describe the data analysis techniques. In Section 3, we present the analysis techniques that we used to investigate variability. We present the results in Section 4, and a discussion and conclusions in Section 5.

## 2. Observations and Data Reductions

The photometric observations were carried out with the 1.26 m NAGIOT at the Xinglong station of the NAOC. This telescope is equipped with three SBIG STT-8300M cameras, whose CCD contains  $3326 \times 2504$  pixels and a field of view of The system enables simultaneous photometry in three optical bands where the three filters adopt the standard Sloan Digital Sky Survey (SDSS)  $g$ ,  $r$ , and  $i$  bands. The aperture radius used for aperture photometry was  $1.2 \times$  FWHM, where FWHM is the average FWHM value of around 10 bright stars in the same frame of BL Lac. For the sky background, we selected a source-free annulus region with an inner and outer radius of  $2.4 \times$  and  $3.6 \times$  FWHM, respectively (for details see Fan et al. 2019). The exact simultaneity of the observations at the three bands is particularly suitable for studying the flux and color variations in blazars.

The observed images contain bias, dark current, flat-field, and target images. We used a 300 s exposure time for each image in all of the bands. The data reduction was carried out using the RAPP (robust automated photometry pipeline; Huang et al. 2020), which includes the following steps. The observed images were corrected for bias, flat and dark current. Then RAPP automatically detects the position of the stars in each image and matches the images based on the information about the position information of the stars. These images were used to create an overlay image, which was later used to register the position of the stars in each CCD image, and the position of a star in different images is obtained. Finally, we carried out the aperture photometry process using the APPHOT package in IRAF<sup>11</sup> software.

We referred to Smith et al. (1985) to obtain the standard stars for this source as listed in Table 1. For all the comparison stars

<sup>11</sup> IRAF is distributed by the National Optical Astronomy Observatories, which are operated by the Association of Universities for Research in Astronomy, Inc., under cooperative agreement with the National Science Foundation.

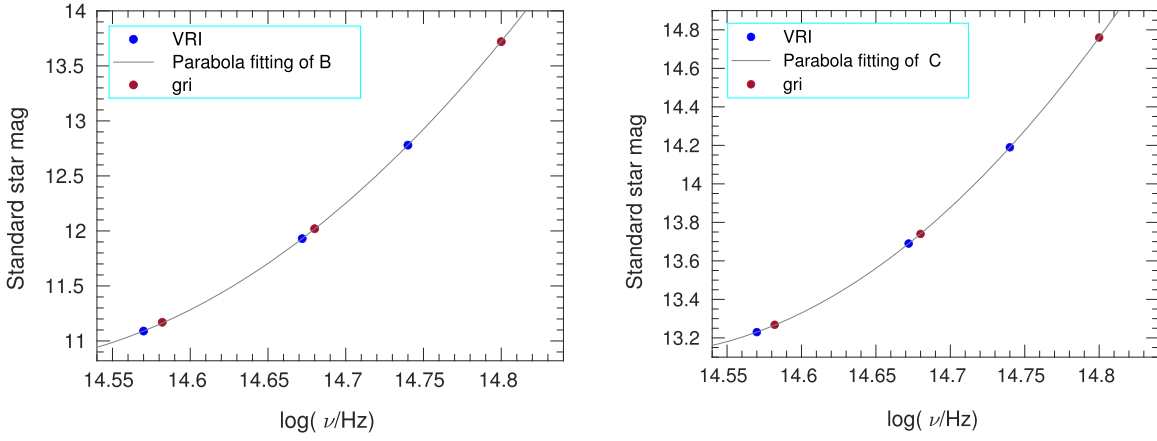


**Figure 1.** The *gri* fitting results of two CSs, B and C, of BL Lac. The black dots denote the *VRI* magnitude, the red dots denote the *gri* fitting results, and the solid line denotes the polynomial fitting lines.

(CSs), based on *VRI* magnitudes, we used a least-squares fitting method to obtain the *gri* magnitudes,  $m_\nu = a \log^2 \nu + b \log \nu + c$ , where,  $m_\nu$  is the magnitude at the  $\nu$  band ( $\nu = V, R$ , and  $I$ ). Figure 1 shows the fitting results, where, the black circles represent *VRI* magnitudes, the red dots stand for *g*, *r*, and *i* magnitudes, and the green curves show the least-squares fitting results.

Following the above method, we extracted the instrumental magnitudes of the source and CSs. The light curves of the source during the observation period on daily and monthly timescales are shown in Figures 2 and 3, respectively. For the calibrated source magnitude, we took the average of the differences between the source and the two CSs, and the corresponding uncertainty was estimated using the error propagation method.

### 3. Statistical Tests Used to Study Variability

In order to detect micro-variation in time-series observations of AGN, several statistical tests have been introduced and used among which the *C*-, *F*- and  $\chi^2$ -tests have been widely used. In addition to these, recently the power-enhanced *F*-test and nested-ANOVA test have been gaining popularity due to their robustness in precisely and accurately detecting microvariability (de Diego 2014; de Diego et al. 2015, see also Gaur et al. 2012; Fan et al. 2021; Kalita et al. 2021). In this study, we used three methods: the *F*-test,  $\chi^2$ -test, and nested-ANOVA test to quantify the variability of the source, which are briefly discussed below.

#### 3.1. *F*-test

In the *F*-test (de Diego 2010), the source differential variance is compared to the differential variance of the CS. The *F*-value is calculated as

$$F_1 = \frac{\text{Var}(\text{BL} - \text{CSA})}{\text{Var}(\text{CSA} - \text{CSB})}, F_2 = \frac{\text{Var}(\text{BL} - \text{CSB})}{\text{Var}(\text{CSA} - \text{CSB})}, \quad (1)$$

where  $\text{Var}(\text{BL}-\text{CSA})$ ,  $\text{Var}(\text{BL}-\text{CSB})$ , and  $\text{Var}(\text{CSA}-\text{CSB})$  are the variances of differential instrumental magnitudes of BL Lac and CSA, BL Lac and CSB, and CSA and CSB, respectively. An average of  $F_1$  and  $F_2$  gives the *F*-value, which is compared with the critical *F*-value,  $F_{\nu_{\text{bl}}, \nu_*}^\alpha$ , where  $\nu_{\text{bl}}$  and  $\nu_*$  are the number of dof for the blazar and CS respectively, calculated as

$(N1)$  with  $N$  being the number of measurements, and  $\alpha$  is the significance level set for the test, which was 99% ( $2.576\sigma$ ) in this case. If the average *F*-value is larger than the critical value, the light curve is variable at a confidence level of 99%.

#### 3.2. $\chi^2$ -test of Variance

In order to check for the presence of variability, we also performed a  $\chi^2$ -test. The null hypothesis is rejected when the statistic exceeds a critical value for a given significance level,  $\alpha$ . The statistic is given as

$$\chi^2 = \sum_{i=1}^N \frac{(V_i - \bar{V})^2}{\sigma_i^2}, \quad (2)$$

where  $\bar{V}$  is the mean magnitude, and  $V_i$  is the magnitude corresponding to the  $i$ th observation having a standard error of  $\sigma_i$ . We took the average of  $\chi^2$ -values obtained from differential magnitudes related to the two CSs. This statistic is then compared with a critical value  $\chi_{\alpha, \nu}^2$  where  $\alpha$  is the significance level set the same as in the *F*-test and  $\nu = N - 1$  is the degree of freedom. A smaller value of  $\alpha$  assures more improbably that the result is produced by chance. The presence of variability is confirmed if  $\chi^2 > \chi_{\alpha, \nu}^2$ .

#### 3.3. Nested-ANOVA Test

In the nested-ANOVA test (de Diego et al. 2015), multiple field stars are used as a reference to estimate the blazar differential photometry without using any CSs. We used groups of replicated observations that compare the dispersion of the individual differential magnitudes of the source within the groups with the one between the groups (discussed in detail in Kalita et al. 2021).

Here, we used two reference stars, the comparison + reference stars used in the previous tests. We divided the time-series observations into different temporal groups,  $n$ , where each group contains  $m = 5$  observations, then we estimated the mean square due to groups ( $MS_G$ ) and due to nested observations in groups ( $MS_{O(G)}$ ) with dof  $\nu_1 = n - 1$  and  $\nu_2 = n(m - 1)$ , respectively. The statistic is given by

$$F = \frac{MS_G}{MS_{O(G)}}, \quad (3)$$

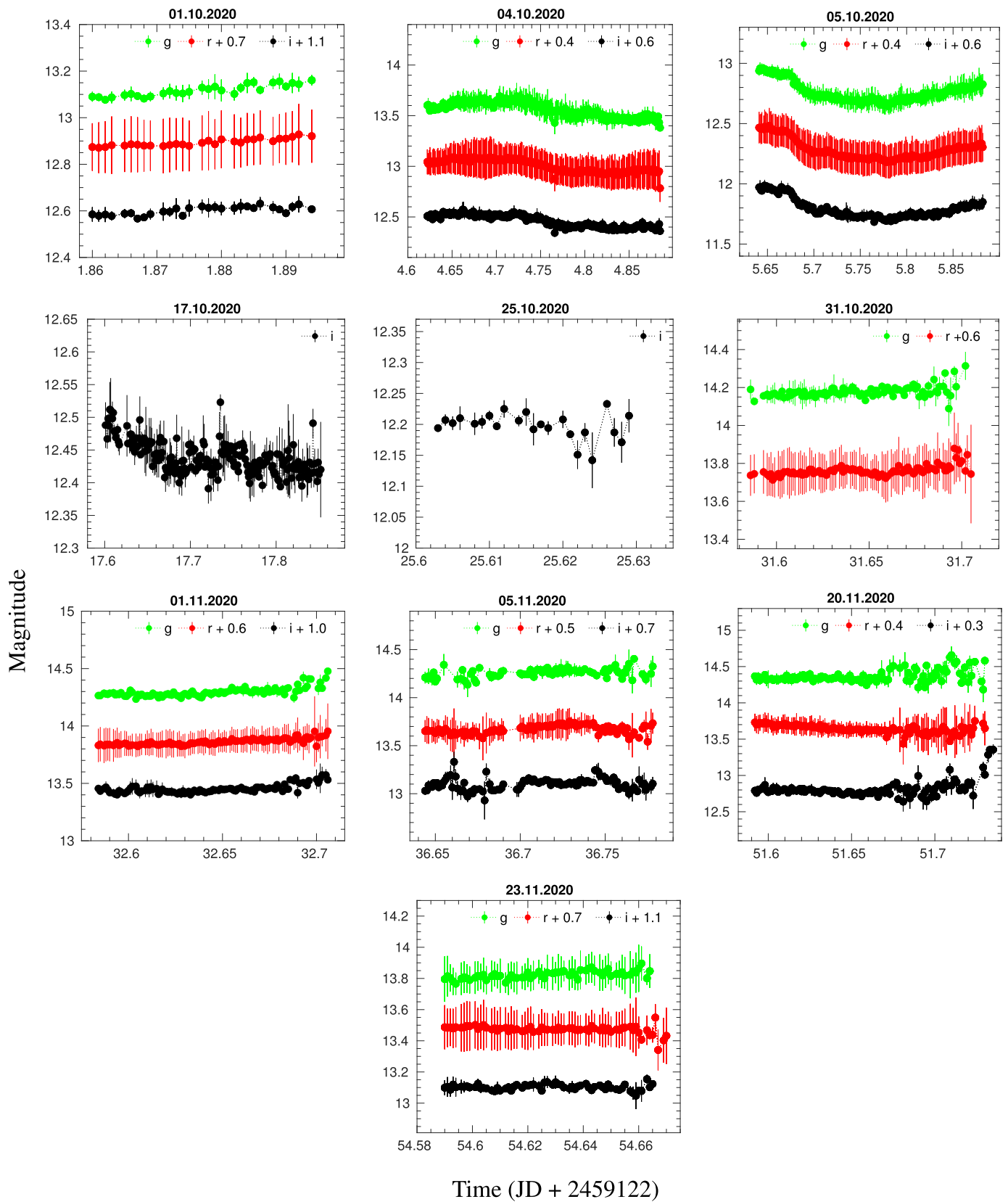


**Figure 2.** Nightly optical light curves of BL Lac in the  $g$ ,  $r$ , and  $i$  filter bands with 100 s binning. On some nights only one (October 17 and 25 or two (October 31) filter band observation was available. The observation dates are shown at the top of each plot.

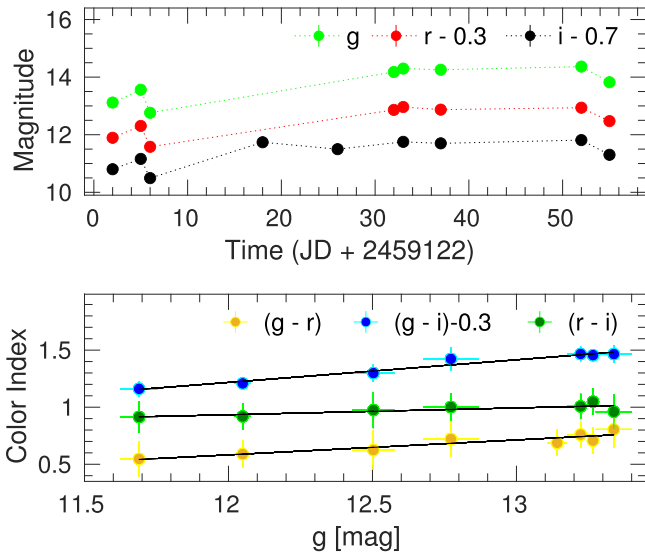


**Figure 3.** Top: long timescale optical  $g$ -,  $r$ -, and  $i$ -band light curves over the whole observation period of BL Lac during 2020 October–November. Bottom: color indices with respect to the  $g$ -band brightness. The black lines represent the least-squares fitting to the data points.

If the  $F$ -value exceeds the critical value  $F_{\nu_1, \nu_2}^{(\alpha)}$  at a significance level of 99% ( $\alpha = 0.01$ ), the null hypothesis will be rejected.

### 3.4. Variability Amplitude

To estimate the variability amplitude of the light curves, we use the variability amplitude defined by Heidt & Wagner (1996) as follows

$$A = \sqrt{(A_{\max} - A_{\min})^2 - 2\sigma^2}, \quad (4)$$

where  $A_{\max}$  and  $A_{\min}$  are the maximum and minimum magnitudes in the blazar light curves and  $\sigma$  is the mean error.

### 3.5. Discrete Correlation Function

To check the correlation between the optical  $g$ ,  $r$ , and  $i$  bands, we applied the discrete correlation function (DCF; Edelson & Krolik 1988), which is one of the best methods to investigate a correlation between two unevenly sampled time-series data. A detailed description of the method we used in this work is given in Kalita et al. (2019). To measure the exact values of the peak and corresponding lag, we fitted the DCF peak with a Gaussian model of the following form:

$$\text{DCF}(\tau) = a \times \exp\left[\frac{-(\tau - m)^2}{2\sigma^2}\right]. \quad (5)$$

Here,  $m$ ,  $a$ , and  $\sigma$  represent the time lag at which the DCF peaks, the peak value of the DCF, and the width of the Gaussian function, respectively.

## 4. Results

### 4.1. Flux and Color Variability

We carried out a variability analysis of the light curves with the  $F$ -test,  $\chi^2$ -test, and nested-ANOVA test, which are discussed in the previous section. IDV results from these three analyses are presented in Table 2. The final remarks on the light curves in Table 2 were made based on  $F$ -statistic values and the

probability of rejecting the null hypothesis estimated from the three methods. If all three statistics were higher than the respective critical values ( $F_{\text{critical}}$  and  $\chi_{\alpha, \nu}^2$ ) at the 99.9% confidence level, then we labeled the light curve as a variable. If any two of the three statistic values were higher than the respective critical values at the 99% confidence level, then it was termed as a probable variable (PV). Finally, the non-variable (NV) one applies when the statistics do not satisfy the above-mentioned conditions.

From our analysis, we detected significant intraday variability near and at the peak of the outburst that took place on October 5. During this phase, the amplitude of the variation reached up to  $\sim 30\%$ . The significant detection of variability decreases toward the end of October. In November, the source showed mixed variability behavior. A significant variation was found on November 20, only in the  $i$ -band light curve. During the observation period, out of 25 intraband light curves, 10 are significantly variable, four are non-variable, and 11 are probably variable. Interestingly, the highest amplitude of variation was found not at or near the outburst peak, but at the end of our monitoring program on November 20 having a value  $\sim 46\%$ . We do not see any frequency-dependent variability from the amplitude analysis.

The variability timescale for intraday flux is estimated using the following formula:

$$t_v = \Delta t \times \frac{\ln 2}{\ln(f_2/f_1)}, \quad (6)$$

where  $f_1$  and  $f_2$  are the flux values at time  $t_1$  and  $t_2$ , and  $\Delta t$  is the difference between  $t_1$  and  $t_2$ . We computed  $t_v$  for all pairs of data points in the light curves and searched for the shortest value in each. The shortest timescale of variability detected for each variable and probably variable light curves are given in Table 2. Since Equation (6) does not include the noise contribution in it, thus, it is possible that it could detect some random outlying points that are close in time, which could give a spurious small  $t_v$  value. In order to avoid such an error we incorporated the error values in Equation (6) with two conditions; we considered all possible pairs of flux values that satisfy the conditions  $f_2 > f_1$  and  $f_2 - f_1 > 3(\sigma_{f_1} + \sigma_{f_2})/2$ , where  $\sigma_{f_1}$  and  $\sigma_{f_2}$  are the uncertainties corresponding to the flux measurements  $f_1$  and  $f_2$ , respectively (Jorstad et al. 2013). Most of the  $r$ -band light curves could not pass the second condition due to the comparatively high error bars in this filter. The inclusion of errors changes the values a little bit and these are listed in the last column of Table 2. On the intraday timescale, we detected a variety of variability timescales ranging from  $\sim 34$  hr to 52 minutes considering both probably variable and variable light curves with an observation period of  $\sim 3$  hr. If we consider only the variable instances from the second estimation, the minimum variability timescale is  $1^{\text{h}}18^{\text{m}}$ . Here again, the shortest variability timescale corresponds not to the outburst peak but to the decaying phase near the end of the monitoring program (see Table 2).

On the LTV timescale, the source was significantly variable in all three bands with variability amplitudes 160.11%, 137.02%, and 132.04% in the  $g$ ,  $r$ , and  $i$  bands, respectively. Unlike on IDV timescales, the source showed clear frequency-dependent variability in this case. The overall brightness variation can be illustrated with  $i$ -band magnitudes as it has the

**Table 2**  
Observation Log and Results of the Analysis of the Variability

Date of Obs. yyyy-mm-dd	Filter Band	Obs. Duration	$F$ -test			$\chi^2$ -test		Nested-ANOVA Test			FVS (9)	$A$ % (10)	$t_v$ (11)	$t_{ve}$ (12)
			dof ( $\nu_1, \nu_2$ ) (1)	$F$ (2)	$F_c$ (3)	$\chi^2$ (4)	$\chi_{\alpha, \nu}^2$ (5)	dof ( $\nu_1, \nu_2$ ) (6)	$F$ (7)	$F_c$ (8)				
2020-10-1	$g$	1 <sup>h</sup> 0 <sup>m</sup>	28	2.84	2.44	263.46	48.28	6, 21	17.45	7.40	V	7.42	6 <sup>h</sup> 37 <sup>m</sup>	76 <sup>h</sup> 00 <sup>m</sup>
	$r$	"	28	3.01	2.44	626.62	"	6, 21	19.06	7.40	V	15.04	9 <sup>h</sup> 40 <sup>m</sup>	NA
	$i$	"	28	1.26	2.44	329.71	"	6, 21	7.82	7.40	PV	5.57	5 <sup>h</sup> 47 <sup>m</sup>	17 <sup>h</sup> 15 <sup>m</sup>
2020-10-4	$g$	6 <sup>h</sup> 20 <sup>m</sup>	218	2.29	1.53	5204.26	269.50	53, 162	37.95	1.66	V	29.37	1 <sup>h</sup> 52 <sup>m</sup>	5 <sup>h</sup> 17 <sup>m</sup>
	$r$	"	218	3.78	1.53	22101.01	"	53, 162	90.45	1.66	V	21.54	1 <sup>h</sup> 14 <sup>m</sup>	NA
	$i$	"	218	4.83	1.53	11734.01	"	53, 162	4.33	1.66	V	22.96	2 <sup>h</sup> 34 <sup>m</sup>	3 <sup>h</sup> 43 <sup>m</sup>
2020-10-5	$g$	5 <sup>h</sup> 50 <sup>m</sup>	200	7.32	1.53	14187.42	249.45	49, 150	153	1.76	V	30.28	3 <sup>h</sup> 15 <sup>m</sup>	33 <sup>h</sup> 57 <sup>m</sup>
	$r$	"	200	41.49	1.53	91965.48	"	49, 150	488.4	1.76	V	23.16	6 <sup>h</sup> 37 <sup>m</sup>	NA
	$i$	"	200	1.92	1.53	62527.53	"	49, 150	2.5	1.76	V	30.14	4 <sup>h</sup> 17 <sup>m</sup>	6 <sup>h</sup> 41 <sup>m</sup>
2020-10-17	$i$	6 <sup>h</sup> 01 <sup>m</sup>	199	1.01	1.53	1247.19	248.33	49, 150	7.12	1.76	V	12.92	2 <sup>h</sup> 44 <sup>m</sup>	3 <sup>h</sup> 56 <sup>m</sup>
2020-10-25	$i$	0 <sup>h</sup> 32 <sup>m</sup>	22	0.60	2.75	93.43	40.29	4, 15	1.53	4.89	NV	...	...	...
2020-10-31	$g$	2 <sup>h</sup> 40 <sup>m</sup>	88	0.60	1.84	263.74	121.77	21, 66	101.20	2.20	PV	19.02	2 <sup>h</sup> 20 <sup>m</sup>	3 <sup>h</sup> 48 <sup>m</sup>
	$r$	"	93	0.86	1.53	459.97	127.63	22, 69	5.57	2.20	PV	6.33	2 <sup>h</sup> 33 <sup>m</sup>	NA
2020-11-1	$g$	2 <sup>h</sup> 50 <sup>m</sup>	98	1.51	1.53	510.55	133.48	23, 72	1.92	2.12	NV	...	...	...
	$r$	"	100	0.66	1.53	1143.73	135.81	24, 75	9.23	2.12	PV	8.32	1 <sup>h</sup> 42 <sup>m</sup>	NA
	$i$	"	99	1.08	1.53	789.46	134.64	24, 75	9.86	2.12	PV	16.78	1 <sup>h</sup> 38 <sup>m</sup>	2 <sup>h</sup> 22 <sup>m</sup>
2020-11-5	$g$	3 <sup>h</sup> 07 <sup>m</sup>	81	0.63	1.84	327.27	113.51	19, 60	1.45	2.20	NV	...	...	...
	$r$	"	99	0.41	1.53	1694.38	134.64	24, 75	4.97	2.12	PV	12.06	1 <sup>h</sup> 20 <sup>m</sup>	5 <sup>h</sup> 50 <sup>m</sup>
	$i$	"	102	0.96	1.53	675.10	138.13	24, 75	4.37	2.12	PV	26.74	0 <sup>h</sup> 41 <sup>m</sup>	2 <sup>h</sup> 10 <sup>m</sup>
2020-11-20	$g$	3 <sup>h</sup> 10 <sup>m</sup>	105	1.35	1.53	401.84	141.62	25, 78	3.81	2.12	PV	46.54	0 <sup>h</sup> 36 <sup>m</sup>	52 <sup>m</sup>
	$r$	"	109	0.39	1.53	2615.49	146.26	26, 81	6.13	2.12	PV	18.77	1 <sup>h</sup> 43 <sup>m</sup>	NA
	$i$	"	112	2.15	1.53	1229.17	149.73	27, 84	7.70	2.03	V	46.46	0 <sup>h</sup> 55 <sup>m</sup>	1 <sup>h</sup> 18 <sup>m</sup>
2020-11-23	$g$	1 <sup>h</sup> 42 <sup>m</sup>	61	0.96	1.84	205.09	89.59	14, 45	4.63	2.52	PV	3.85	3 <sup>h</sup> 46 <sup>m</sup>	5 <sup>h</sup> 26 <sup>m</sup>
	$r$	"	66	0.44	1.84	406.99	95.63	15, 48	0.10	2.52	NV	...	...	...
	$i$	"	62	0.47	1.84	314.73	90.80	14, 45	3.98	2.52	PV	9.97	3 <sup>h</sup> 46 <sup>h</sup>	5 <sup>h</sup> 30 <sup>m</sup>

**Note.** Column (1): dof in the  $F$ -statistic and  $\chi^2$ -distribution. (dof+1) represents the number of data points obtained during each night; Column (2):  $F$ -value for the  $F$ -test; Columns (3) and (8): the critical values at 99.9% ( $F_c$ ); Column (6): dof in the numerator and the denominator in the ANOVA statistics; Column (7):  $F$ -value for the nested-ANOVA test; Column (9): final variability status ( $V$  = variable;  $NV$  = non-variable;  $PV$  = probable variable); Column (10): amplitude of variation; Column (11): timescale of variability; Column (12):  $t_{ve}$  estimated incorporating errors.

most observation nights. In the beginning, on October 1, the source brightness was 11.5 mag, which decreased to 11.9 on October 4 followed by brightening to 11.2 mag on October 5, the peak of the overall light curve in our observation session. A concave light curve was detected on October 5, in the way that the source brightness gradually increased from 11.4–11.1 mag, then decreased to about 11.2 mag (see Figure 2). After that, the source stayed relatively stable at a faint state ( $\sim$ 12.2–12.5 mag), and finally, brightened to  $\sim$ 12 mag on the last night of our observation session (see Figure 3). Overall during this period, the brightness changed by 1.3 mag from a minimum of 12.5 to a maximum of 11.2. On a long timescale, the estimated  $t_v$  values are 11.41, 11.72, and 11.97 days for the  $g$ ,  $r$ , and  $i$  bands, respectively with or without including errors in Equation (6).

In a correlation analysis, we measured the DCF values between the  $g$  and the other two bands using a binning size of 5, which is equivalent to a time difference of  $\sim$ 7 minutes. We found that all the optical bands are nicely correlated to each other with DCF peaks at  $\approx$ 0.80–0.95, i.e., with 80%–95% degrees of correlation, having a DCF curve similar to that shown in Figure 4. In this case, the cross-correlation is very nearly symmetrical around zero lag, which is almost identical to an autocorrelation, explicitly indicating simultaneous emission of all the optical bands from the same electron population and radiation zone.

#### 4.2. Spectral Variation with Color–Magnitude Diagram

In order to study the spectral behavior of the outburst event, we investigated the color–magnitude diagrams (CMDs) of the  $g$ - $r$ ,  $g$ - $i$ , and  $r$ - $i$  color indices versus the  $g$ -band magnitude. The magnitudes were corrected for Galactic extinction using the values taken from the NASA/IPAC Extragalactic Database<sup>12</sup> (NED; Schlegel et al. 1998). Since BL Lac is hosted by a relatively bright galaxy, we subtracted its contribution from the observed fluxes in order to avoid contamination in the color indices. According to Scarpa et al. (2000), the  $R$ -band magnitude of the BL Lac host galaxy is  $R_{\text{host}} = 15.55 \pm 0.02$  and by taking the average color indices for elliptical galaxies with  $M_V < -21$  from Mannucci et al. (2001), we estimated the host galaxy brightness in other bands. These Johnson filter band magnitudes are then converted into SDSS filter magnitudes following the steps given on the SDSS website<sup>13</sup> (Jester et al. 2005) and then corrected for the host reddening using the Galactic extinction coefficient values given in NED. These dereddened magnitudes are converted into SDSS fluxes using the method given on the SDSS website. The resulting host galaxy fluxes in the  $g$ ,  $r$ , and  $i$  bands are 2.62, 2.48, and 2.91 mJy, respectively. If we consider the source extraction radius (following Villata et al. 2002; Raiteri et al. 2009) used in

<sup>12</sup> <https://ned.ipac.caltech.edu/>

<sup>13</sup> <https://www.sdss3.org/dr8/algorithms/sdssUBVRITransform.php>

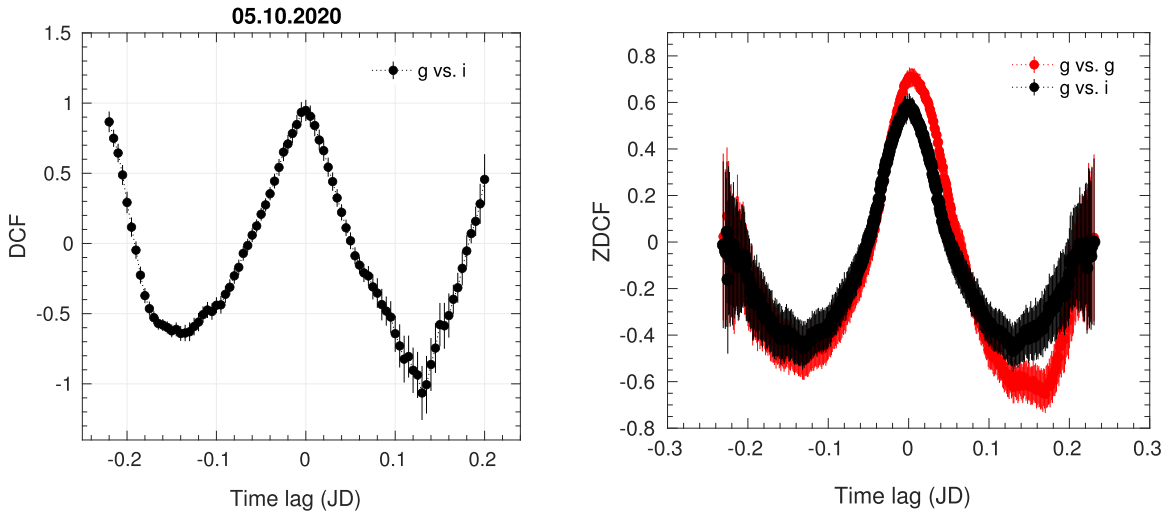


**Figure 4.** An example of a correlation between the  $g$  and  $i$  bands using the DCF method is shown in first panel. The second panel shows the  $z$ -transformed DCF relation estimated using the code provided by Alexander (1997) where we used binning of 60, and uniform sampling of the light curve. Errors were estimated via Monte Carlo error approximation. The plot includes all the data points. Both tests show a similar correlation pattern.

this study, the host galaxy contribution to the observed flux is about 50% of the total galaxy flux. This contribution was removed from both the observed magnitudes and fluxes for color and spectral studies.

The CMD plots are presented in Figure 5. As can be seen in the figure, most of the plots show a positive correlation characterized by hardening of the optical continuum with increasing brightness, a trend popularly known as BWB. Only in a few cases, an opposite trend is observed i.e., steepening of the continuum with brightness, also known as redder when brighter (RWB). To quantify these correlations, we performed a linear regression fit on each plot using the least-squares method. The fitting is shown by a black straight line in the plots. We considered it as significant only if the derived probability of rejecting the null hypothesis,  $p$ -values  $\geq 0.01$  (i.e. 99% significance level). This way, 72% of instances exhibit significant correlations and all of them follow a BWB trend. However, it is worth mentioning that 96% of the light curves show a BWB trend, and the rest shows a very weak RWB pattern. All the fitting results are listed in Table 3. Overall, the  $r-i$  color correlations to the  $g$  band are weaker than the rest, and those that show weak RWB trends belong to this color index, but this pattern only appears in the later observation taken in November. We noticed that the color analysis is not affected much by the host galaxy contribution and Galactic extinction.

In the CMD for October 4 (Figure 5), the night before the peak night we notice that the  $g-r$  and  $g-i$  color indices cluster in two different branches at a particular brightness ( $\sim 12.49$  mag), one below the other showing an overall BWB trend. For a clear representation, we plot only the  $g-i$  data points against the  $g$ -band magnitude in the first panel of Figure 6. We omit the error bars for better visibility. In this figure, the two branches (red and yellow points), which belong to two different epochs, clearly stand out. The branches represent two distinct spectral states, which appear within only 6 hr and 20 minutes of the observation time. The second branch appears after  $\sim 3$  hr. The  $R$ -values obtained from separate fitting to the red and yellow branches are 0.82 and 0.74 with slopes of 0.70 and 0.73, respectively. When we fit the overall data, it gives a very weak correlation with a small  $R$ -value as compared to the separate fitting values. The time evolution of color is a bit complicated

rather than gradual as can be seen in the second panel of the figure. Although there is distinct branching of the colors, it seems the colors do not particularly follow a clean pattern with time within the individual branches.

From the CMD, the average spectral indices of the optical spectrum can be derived simply by using the average colors ( $g-r$ ,  $g-i$ , and  $r-i$ ) (Wiercholska et al. 2015) as

$$\langle \alpha_{gr,gi,ri} \rangle = \frac{0.4 \langle g-r, g-i, r-i \rangle}{\log(\nu_{g,r}/\nu_{r,i})}, \quad (7)$$

where  $\nu_{g,r}$  and  $\nu_{r,i}$  are effective frequencies of the respective bands (Bessell et al. 1998). The estimated values are listed in Table 3.

The Galactic reddening- and host-corrected color indices versus  $g$ -band magnitudes during the entire observation period is shown in the bottom panel of Figure 3. A least-squares fitting to the  $g-r$ ,  $g-i$ , and  $r-i$  colors gives slopes of 0.13, 0.20, and 0.06 with correlation coefficient,  $R$ -values 0.92, 0.98, and 0.79, respectively, which represent even stronger correlations than that is observed in the respective colors for intraday timescales. The corresponding spectral slopes estimated using Equation (7) are  $3.39 \pm 0.46$ ,  $3.47 \pm 0.14$ , and  $3.58 \pm 0.63$ , respectively. From these data, we can say that the long-term flux oscillations are as strongly chromatic as that in fast flux changes and follow a strong BWB trend.

### 4.3. SEDs

SEDs were developed with the  $gri$  bands using the average fluxes in individual energy bands for each night. Figure 7 shows the SEDs in the  $\log(\nu F_\nu)$  versus  $\log \nu$  representation for seven out of the total 10 observation nights, for which data are available in all three bands. The optical emission of blazars generally follows a power-law shape of the form  $F_\nu \propto \nu^{-\alpha}$ , where  $\alpha$  is the spectral index. Using this model, we extracted the optical spectral slopes for each night, which range from 0.82, corresponding to the hardest spectra observed on the night of the outburst peak, to 1.44, the softest spectra detected on November 20. During our monitoring period, the slope varies by  $\Delta\alpha = 0.62$  having a mean value of 1.2 where the bluest spectrum corresponds to the highest flux state of the

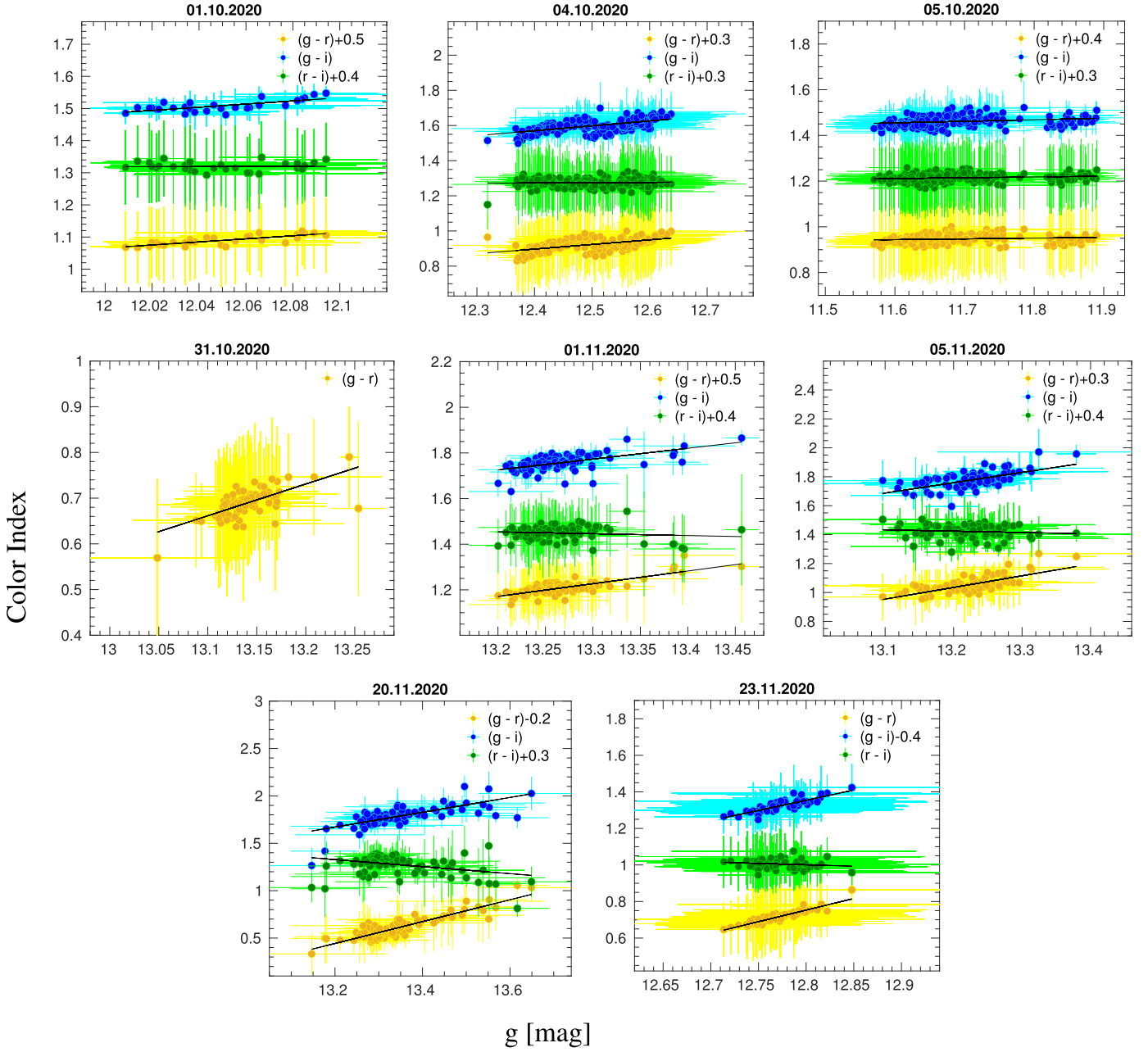


**Figure 5.** Color indices vs.  $g$ -band magnitude plots on an intranight timescale. observation dates are given at the top of each plot. The black lines represent a least-squares fitting to the data points. Magnitudes used here are corrected for Galactic reddening and host galaxy contamination.

source and the spectral hardness is strictly dependent on brightness. These values are listed in Table 3.

In order to further explore how the optical emission evolved with time on the night of October 4, we developed the  $gri$  bands' SEDs in a time interval of 15 minutes, i.e., the data points in a given SED represent the average of data acquired within 15 minutes of exposure. For the SED fittings, we follow the same process explained above and extracted the spectral indices, which range between 1 and 1.2. The variation of spectral indices throughout the night with time is shown in Figure 8, where the vertical line represents the epoch where the double spectral state starts to appear as shown in Figure 6. A polynomial of the form of  $y = ax^2 + bx + c$  can well represent

the underlying spectral evolution trend of the night, which is shown by the red curve in the figure. The model coefficients are  $a = -8.6893$ ,  $b = 82.409$ , and  $c = -194.2485$ .

## 5. Summary and Discussion

The study of optical flares is extremely useful to get an in-depth understanding of the evolution of hidden physical processes that trigger or sustain them as they take longer timescales to develop than their corresponding higher energy counterparts, thus containing more structure to study. The historical high outburst of the prototype blazar BL Lac gives us an excellent window to examine such events in detail. In this paper, we carried out a study to understand the optical behavior

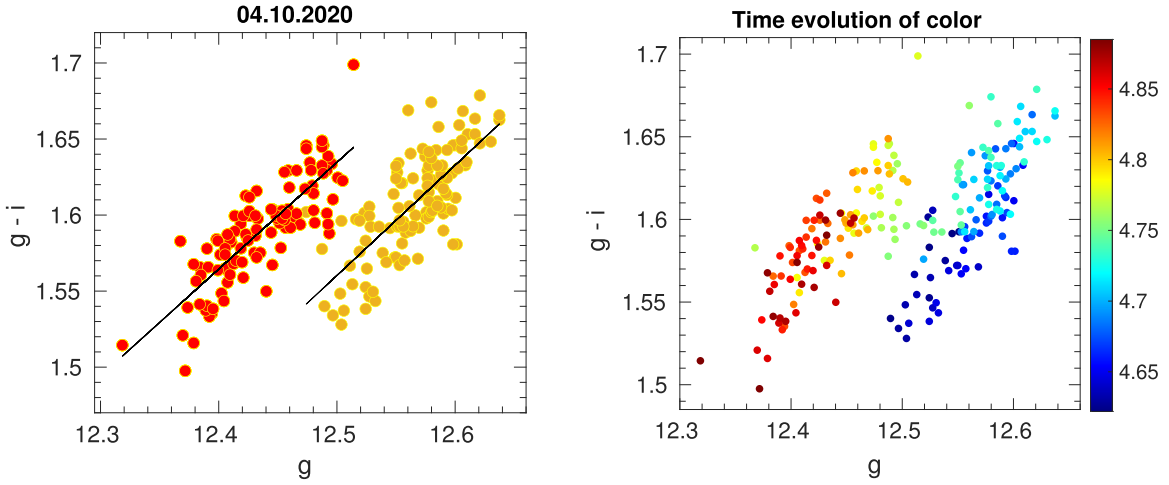


**Figure 6.** We note two distinct optical spectral states appearing within  $\sim 6$  hr on 2020 October 4, the night before the source reached its first historical maxima in the optical band. A least-squares fitting to the time-separated data sets shown by the black lines gives Pearson’s correlation coefficients of 0.82 and 0.73, respectively, shown by red and yellow symbols in the first panel. The error bars are omitted to get a clearer view of the spectral states. The second panel shows the time evolution of color, where the right-hand side color bar represents time in the unit of  $+2459122$  MJD.

of the blazar BL Lac during its outburst in 2020. We studied the flaring event on the temporal and spectral domains on intraday and long timescales using multi-band optical observations from 2020 October to November.

From our time-series analysis, we found that the source was significantly variable on both intranight and long timescales during the observation period with high amplitude of variation on long timescales than that on intranight timescales. We found that the source showed a variety of variability timescales on different nights from minutes to hours. The minimum timescale can be related to the size  $l$  of the emitting feature in the jet (e.g., Romero et al. 1999):

$$l \sim t_v c \gamma^2 (1+z)^{-1}, \quad (8)$$

where  $\gamma = (1 - \beta^2)^{-1/2}$  is the Lorentz factor of the shock and  $z$  is the redshift. If we assume a small viewing angle of the jet, which is the case in a blazar ( $\cos \theta \sim \beta$ ), we can replace the Lorentz factor  $\gamma$  in the equation with the Doppler factor  $\delta = [\gamma(1 - \beta \cos \theta)]^{-1}$ . Assuming a typical value of  $\delta \sim 10$ , we get the emitting feature size  $l \sim 4 \times 10^{-3}$  pc from the minimum timescales estimated by considering only variable instances. The highest variability timescale belongs to a size of  $\sim 6.7$  pc on the IDV timescale. The compactness of the size of the emitting regions indicates that these variations are similar to light-crossing time in  $\sim 100 R_s$  of the central black hole ( $\sim 2 \times 10^8 M_\odot$ ; Woo & Urry 2002), which comes from some mini-structures within the jet.

In the context of the shock-in-jet model, the size or thickness of the emitting zone increases with the distance traveled by the shock along the jet (Blandford & McKee 1976). An emitting region in the order  $\times 10^{-3}$  pc estimated above means that the shock-feature interaction must be occurring very close to the jet’s apex. The asymmetric flux variation on the nightly timescale observed in BL Lac in this study most likely resulted from some random processes, such as the stochastic acceleration process in a turbulent region behind the shock front. During the event, the timescale of variability was even faster ( $\sim 1$  m) in the X-ray band suggesting an even smaller size for the emitting region (D’Ammando 2022). When QPOs were in

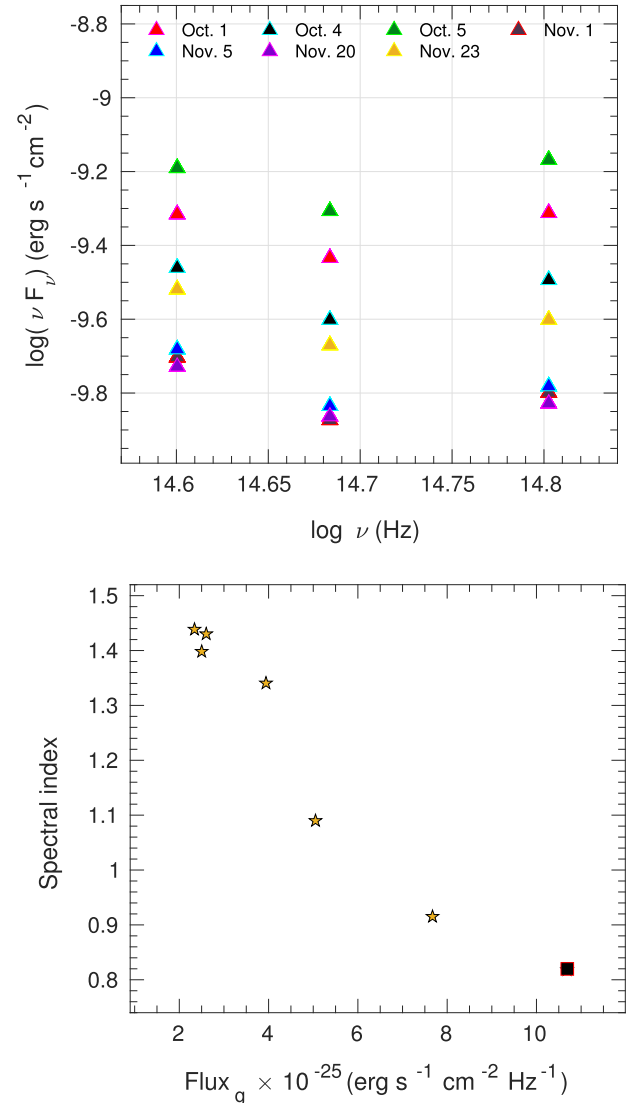


**Figure 7.** Top panel: optical intranight SEDs of BL Lac during our observation period. Dates are given at the top of the plot. Bottom panel: spectral slope and  $g$ -band flux relationship. The square point represents the outburst peak.

**Table 3**  
Results of Color and SED Analysis

Date yyyy-mm-dd	Color	$R$ (1)	$P$ (2)	$a$ (3)	$\alpha_{gr,gi,ri}$ (4)	$\alpha_{sed}$ (5)
2020-10-1	$g-r$	0.80	2.46e-07	0.48	$3.10 \pm 0.39$	0.92
	$g-i$	0.70	1.76e-05	0.49	$3.19 \pm 0.08$	"
	$r-i$	0.03	8.96e-01	0.01	$3.33 \pm 0.56$	"
2020-10-4	$g-r$	0.58	4.04e-21	0.26	$3.21 \pm 0.59$	1.09
	$g-i$	0.60	7.50e-23	0.28	$3.37 \pm 0.17$	"
	$r-i$	0.05	4.26e-01	0.02	$3.59 \pm 0.77$	"
2020-10-5	$g-r$	0.15	3.67e-2	0.03	$2.96 \pm 0.51$	0.82
	$g-i$	0.25	4.71e-4	0.07	$3.11 \pm 0.14$	"
	$r-i$	0.18	1.19e-2	0.04	$3.31 \pm 0.67$	"
2020-10-31	$g-r$	0.66	2.87e-12	0.70	$3.42 \pm 0.47$	"
2020-11-1	$g-r$	0.78	6.49e-21	0.56	$3.48 \pm 0.39$	1.40
	$g-i$	0.57	6.22e-10	0.48	$3.65 \pm 0.09$	"
	$r-i$	-0.12	2.28e-01	-0.08	$3.90 \pm 0.57$	"
2020-11-5	$g-r$	0.72	1.85e-14	0.80	$3.62 \pm 0.41$	1.43
	$g-i$	0.62	4.29e-10	0.71	$3.69 \pm 0.14$	"
	$r-i$	-0.10	3.60e-01	-0.09	$3.78 \pm 0.56$	"
2020-11-20	$r$	0.89	2.59e-37	1.15	$3.78 \pm 0.60$	1.44
	$g-i$	0.71	3.18e-17	0.78	$3.69 \pm 0.19$	"
	$r-i$	-0.35	2.12e-04	-0.37	$3.56 \pm 0.82$	"
2020-11-23	$g-r$	0.92	3.11e-26	1.27	$3.52 \pm 0.52$	1.34
	$g-i$	0.84	1.62e-17	1.11	$3.60 \pm 0.20$	"
	$r-i$	-0.16	2.20e-01	-0.16	$3.72 \pm 0.60$	"

**Note.** Column (1): Pearson correlation coefficient; Column (2): probability of rejecting the null hypothesis; Column (3): slope of least-squares fitting; Column (4): average spectral indices of the optical spectrum; Column (5): spectral slope estimated from SED fitting.

optical flux and polarization,  $\gamma$ -ray flux with cycles of 13 hr was also detected (Jorstad et al. 2022).

On a longer timescale, taking the average values of  $t_v$ , we found an emitting region of size  $\sim 55.07$  pc. Unlike the IDV, the LTV shows frequency-dependent behavior. Also, the variability timescales for the  $g$ ,  $r$ , and  $i$  bands are systematic while we found chaotic timescales for the three energy bands on the same night on intranight timescales. These opposite behaviors clearly indicate that the emission on the two timescales is governed by completely different processes. In previous studies, different emission processes resulting in the faster and longer timescale variability were reported for BL Lac where the chromatic faster variability and the mildly chromatic or achromatic longer variability have been linked with the substructure in a shock-induced jet and changes in the Doppler factor, respectively (Villata et al. 2002, 2004; Raiteri et al. 2009, 2013). Our results are similar to the previous one on intranight timescales; however, unlike on previous occasions, this time the source showed a strong BWB trend or chromatism on longer timescales as well. Considering the symmetric variability timescales for LTV and the parsec scale size ( $\sim 55$  pc) of the emitting region, we can say that the LTV likely originated from an external jet region via a systematic process.

The absence of time lags between intra-optical bands is expected as they are very close in the energy domain, and in case any lags are present, they must be insignificant and shorter than the resolution of the light curves. Simultaneous and correlated emission of the optical band and  $\gamma$ -rays were also detected during the event, indicating cospatiality of the emitting regions (Jorstad et al. 2022). However, BL Lac was found to show correlated variability with a hard lag of approximately

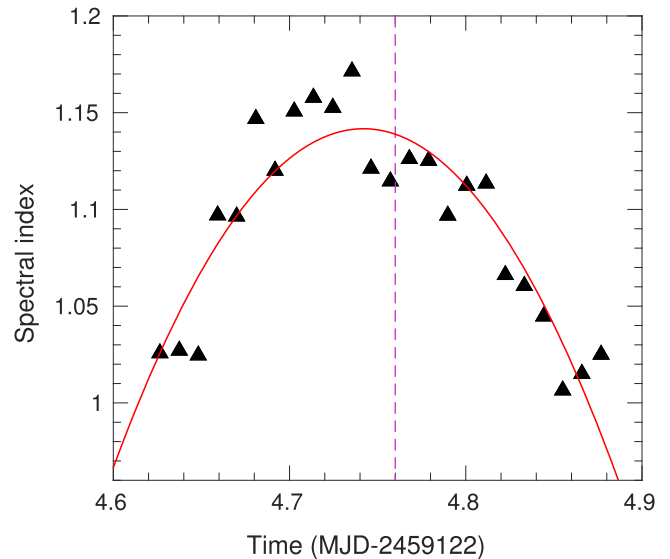


**Figure 8.** Spectral index evolution on October 4. Slopes were estimated by fitting the SEDs with a simple power-law model ( $F_\nu \propto \nu^{-\alpha}$ ). The vertical dashed line represents the epoch where the double spectral states start to appear (see Figure 6). The spectral evolution throughout the night can be fitted with a second-degree polynomial shown by the red curve.

1 day between the X-rays and other energy bands in a study by Prince (2021). In a shock-induced flare, the higher energy (HE) emission peaks first, which are followed by optical, IR, and then radio, referred to as soft lag, which are commonly observed in blazars, and are explained by cooling of HE particles gradually radiating on lower and lower frequencies. However, an opposite pattern called as hard lags, i.e., the HE photons lag behind the soft, has also been observed in a few well-known HBLs; Mrk 401, Mrk 501, and PKS 2155–304 (Zhang et al. 2002; Brinkmann et al. 2005; Tammi & Duffy 2009; Abeysekara et al. 2017). This type of observed delay requires the emitting particles within the jet to get heated or accelerated during the flare instead of getting cooled off via radiation (Mastichiadis & Moraitis 2008). One possible reason could be the generation of turbulence, especially the nonlinear one by the particles themselves, which could be efficient in triggering the fast acceleration that leads to hard lags (Tammi & Duffy 2009). In the context of particle acceleration within a shocked region, soft lags are expected when cooling timescales ( $t_{cool}$ )  $\gg$  acceleration timescales ( $t_{acc}$ ) of the relativistic particles, and we observe hard lag when  $t_{cool} \sim t_{acc}$  (an in-depth discussion is given in Zhang et al. 2002). The particles could be accelerated to relativistic speed by the first-order Fermi acceleration in the presence of an ordered magnetic field at a shock front and/or by the second-order Fermi acceleration, also known as the stochastic acceleration process due to plasma turbulence resulting from a chaotic magnetic field in a downstream region of the shock, and/or by multiple magnetic reconnections (Katarzyński et al. 2006).

Another potential explanation for the observed variability behavior is magnetic reconnection inside a magnetically dominated jet (Mizuno et al. 2011; Sironi et al. 2015; Petropoulou et al. 2016). When the traveling shock interacts with the inhomogeneous medium, turbulence would be created behind the shock front by hydrodynamical instability (e.g., Mizuno et al. 2011, 2014). The turbulence would locally amplify the magnetic field as filamentary structures. A

turbulent plasma with fast-moving magnetic filaments is likely a site for second-order Fermi acceleration of charged particles. Magnetic-reconnection events are expected to take place as the turbulent magnetic field behind the shock front would become progressively stronger due to the continuous interaction of the traveling shock with its inhomogeneous medium. A strong magnetic reconnection could produce mini-jets, that are similar to the jet-in-jet model (Giannios et al. 2009). In this scenario, a large amount of magnetic energy is released whenever opposite polarity magnetic field lines interact with each other, which energized the intervening plasma, and thus, accelerates the particles resulting in the observed systematic fast variability and hard lags. During the outburst of BL Lac, a kink in the jet at 43 GHz was observed by Jorstad et al. (2022), which yields the presence of a tight helical magnetic field. The authors described the detected QPOs as a result of current-driven kink instabilities near a recollimation shock that was produced from pressure mismatches between the jet and its surroundings. The systematic LTV pattern on the parsec scale that we observed in our study is most likely a result of this helical magnetic field.

The spectral evolution during the outburst phase shows strong BWB chromatism, which is observed during the entire observation period, except in four cases of  $r$ - $i$  color where a weak opposite pattern appeared in the later part of our observations. The absence of the RWB in other colors on the same nights makes us uncertain about these results. The color index and magnitude relation are governed by contributions made by the jet and the disk toward the overall optical emissions (Raiteri et al. 2009; Bonning et al. 2012). The accretion disk component is inherently bluer and stable, while the jet contribution is variable and redder. The observed BWB states of the source are likely a result of significantly less radiative cooling of highly accelerated electrons over an under-luminous accretion disk. An interesting finding of this work is the detection of separate optical states on a single night observation. On October 4, the color indices corresponding to two epochs separated by an  $\sim 3$  hr cluster in two distinct branches on the CMD both following the BWB trend with similar slopes at a high significance of correlation; however, the colors of the two branches are clearly different with the bright branch being systematically redder than the faint one. This is the shortest period ever detected exhibiting such a pattern. A weak similar type of detection was reported for the blazar PKS 2155-304 over a years long period, while the source was transitioning from a flaring to a quiescent state (H. E. S. S. Collaboration et al. 2014). The authors related the observed pattern to distinct  $\gamma$ -ray states, where complex scaling between the optical and  $\gamma$ -ray emission exists. In the study, they found that the  $\gamma$ -ray flux depends on a combination of optical flux and color rather than flux alone.

While both results were found at a high optical flux state, our finding differs from theirs twofold. First, the timescale is completely different. Two tracks in this work were found in a very short period of about 6 hr, while theirs were based on a comparison with the well-separated months-long variations in years. Second, our two tracks transited at  $g \sim 13.55$ , around which the source brightness was gradually changing from  $g \sim 13.6$  to  $g \sim 13.5$  (see Figure 2), and there is not much overlapping flux. In contrast, the two color trends in PKS 2155-304 have a large portion of overlapped flux states (see their Figure 1). It seems that in our source, a physically distinct event happened when the source gradually brightened to  $g \sim 13.55$ . It is likely that we were witnessing a new jet ejection event on the night of 2020 October 4. While the ejection increases the source brightness, due to some

reason, the new ejection has a softer electron energy distribution than the previous one, which results in two tracks in the CMD, although both of them follow the BWB trend.

The spectral evolution pattern we see from the time-resolved spectral fit shown in Figure 8 follows a hard-soft-hard (HSH) trend, that is, the spectra evolve from hard to soft and then back to a hard state again. Such an HSH trend was found in solar flares in X-rays at higher energies, which are suggested to be a general trend of nonthermal emissions throughout flares with individual peaks in the emission within a single flare (Shao & Huang 2009). In this scenario, particle trapping either by stochastic acceleration or wave scattering in MHD turbulent regions leads to enhanced high-energy emission versus low-energy emission in between acceleration episodes (Aschwanden 2002). Hence, the HSH-pattern spectra may be associated with multiple injections of nonthermal electrons. Any small sub-peak may denote a new injection to soften the original spectra, and the spectra are hardened again afterward (Melnikov & Magun 1998). To check this scenario and its applicability in blazar flares, however, requires more sensitive and statistically strong data than we have, as well as further elaborated studies.

We thank the anonymous referee for the comments and suggestions that made the manuscript more comprehensive. I would like to thank C.M. Raiteri for the valuable discussion. The work by N.K. is partially supported by the Chinese Academy of Sciences (CAS) Presidents International Fellowship Initiative (PIFI) grant No. 2020PM0029. N.K., P.J., H.Z., and X.P. acknowledge support from the Natural Science Foundation of Shanghai (20ZR1463400, 20ZR1473600, 21ZR1469800). M.F.G. acknowledges support from the National Science Foundation of China (NSFC; grant 11873073), Shanghai Pilot Program for Basic Research—CAS, Shanghai Branch (JCYJ-SHXY-2021-013), and the science research grants from the China Manned Space Project with grant No. CMSCSST-2021-A06. J.H.F. acknowledges support from the NSFC (U2031201 and 11733001) and the Guangdong Major Project of Basic and Applied Basic Research (grant No. 2019B030302001). A.C.G. is partially supported by the CAS PIFI (grant no. 2016VMB073). A.A.S. and R.S.B. acknowledge support from the Bulgarian National Science Fund of the Ministry of Education and Science under grants KP-06-H28/3 (2018), KP-06-H38/4 (2019), KP-06-KITAJ/2 (2020), and KP-06-PN68/1(2022).

## ORCID iDs

Nibedita Kalita  <https://orcid.org/0000-0002-9323-4150>  
 Yuhai Yuan  <https://orcid.org/0000-0001-7833-2468>  
 Minfeng Gu  <https://orcid.org/0000-0002-4455-6946>  
 Junhui Fan  <https://orcid.org/0000-0002-5929-0968>  
 Yosuke Mizuno  <https://orcid.org/0000-0002-8131-6730>  
 Alok C. Gupta  <https://orcid.org/0000-0002-9331-4388>  
 Xiang Pan  <https://orcid.org/0000-0002-6565-2339>  
 Rumen S. Bachev  <https://orcid.org/0000-0002-0766-864X>  
 Lang Cui  <https://orcid.org/0000-0003-0721-5509>

## References

- Abdo, A. A., Ackermann, M., Ajello, M., et al. 2011, *ApJ*, 730, 101  
 Abeyskara, A. U., Archambault, S., Archer, A., et al. 2017, *ApJ*, 834, 2  
 Ackermann, M., Ajello, M., Allafort, A., et al. 2011, *ApJ*, 743, 171  
 Agarwal, A., & Gupta, A. C. 2015, *MNRAS*, 450, 541

- Albert, J., Aliu, E., Anderhub, H., et al. 2007, *ApJL*, **666**, L17
- Alexander, T. 1997, in *Astronomical Time Series*, ed. D. Maoz, A. Sternberg, & E. M. Leibowitz, Vol. 218 (Dordrecht: Springer), 163
- Arlen, T., Aune, T., Beilicke, M., et al. 2013, *ApJ*, **762**, 92
- Aschwanden, M. J. 2002, *Particle Acceleration and Kinematics in Solar Flares*, Vol. 101 (Dordrecht: Springer)
- Bach, U., Villata, M., Raiteri, C. M., et al. 2006, *A&A*, **456**, 105
- Bessell, M. S., Castelli, F., & Plez, B. 1998, *A&A*, **333**, 231
- Bhatta, G., & Webb, J. 2018, *Galax*, **6**, 2
- Blanch, O. 2020, *ATel*, **13963**, 1
- Blandford, R. D., & McKee, C. F. 1976, *PhFI*, **19**, 1130
- Bonning, E., Megan Urry, C., Baily, C., et al. 2012, *ApJ*, **756**, 13
- Böttcher, M., Marscher, A. P., Ravasio, M., et al. 2003, *ApJ*, **596**, 847
- Brinkmann, W., Papadakis, I. E., Raeth, C., Mimica, P., & Haberl, F. 2005, *A&A*, **443**, 397
- Capetti, A., Raiteri, C. M., & Buttiglione, S. 2010, *A&A*, **516**, A59
- Cheung, C. C. 2020, *ATel*, **13933**, 1
- Cohen, M. H., Meier, D. L., Arshakian, T. G., et al. 2015, *ApJ*, **803**, 3
- Corbett, E. A., Robinson, A., Axon, D. J., et al. 1996, *MNRAS*, **281**, 737
- D'Ammando, F. 2021, *ATel*, **14342**, 1
- D'Ammando, F. 2022, *MNRAS*, **509**, 52
- de Diego, J. A. 2010, *AJ*, **139**, 1269
- de Diego, J. A. 2014, *AJ*, **148**, 93
- de Diego, J. A., Polednikova, J., Bongiovanni, A., et al. 2015, *AJ*, **150**, 44
- Edelson, R. A., & Krolik, J. H. 1988, *ApJ*, **333**, 646
- Fan, J.-H., Yuan, Y.-H., Wu, H., et al. 2019, *RAA*, **19**, 142
- Fan, J. H., Yang, J. H., Liu, Y., et al. 2016, *ApJS*, **226**, 20
- Fan, J. H., Kurtanidze, S. O., Liu, Y., et al. 2021, *ApJS*, **253**, 10
- Gaur, H., Gupta, A. C., Wiita, P. J., et al. 2014, *ApJL*, **781**, L4
- Gaur, H., Gupta, A. C., Strigachev, A., et al. 2012, *MNRAS*, **420**, 3147
- Gaur, H., Gupta, A. C., Bachev, R., et al. 2015, *MNRAS*, **452**, 4263
- Giannios, D., Uzdensky, D. A., & Begelman, M. C. 2009, *MNRAS*, **395**, L29
- Gómez, J. L., Lobanov, A. P., Bruni, G., et al. 2016, *ApJ*, **817**, 96
- Grishina, T. S., & Larionov, V. M. 2020, *ATel*, **13930**, 1
- Gu, M. F., Lee, C.-U., Pak, S., Yim, H. S., & Fletcher, A. B. 2006, *A&A*, **450**, 39
- Gupta, A. C., Banerjee, D. P. K., Ashok, N. M., & Joshi, U. C. 2004, *A&A*, **422**, 505
- H. E. S. S. Collaboration, Abramowski, A., Aharonian, F., et al. 2014, *A&A*, **571**, A39
- Hagen-Thorn, V. A., Larionov, E. G., Jorstad, S. G., Björnsson, C.-I., & Larionov, V. M. 2002, *A&A*, **385**, 55
- Heidt, J., & Wagner, S. J. 1996, *A&A*, **305**, 42
- Huang, W., Xie, Z., Zhong, W., et al. 2020, *PASP*, **132**, 075001
- Jester, S., Schneider, D. P., Richards, G. T., et al. 2005, *AJ*, **130**, 873
- Jorstad, S. G., Marscher, A. P., Smith, P. S., et al. 2013, *ApJ*, **773**, 147
- Jorstad, S. G., Marscher, A. P., Raiteri, C. M., et al. 2022, *Natur*, **609**, 265
- Kalita, N., Gupta, A. C., & Gu, M. 2021, *ApJS*, **257**, 41
- Kalita, N., Sawangwit, U., Gupta, A. C., & Wiita, P. J. 2019, *ApJ*, **880**, 19
- Katarzyński, K., Ghisellini, G., Mastichiadis, A., Tavecchio, F., & Maraschi, L. 2006, *A&A*, **453**, 47
- Kunkel, L., Scherbantini, A., Mannheim, K., et al. 2021, *ATel*, **14820**, 1
- MAGIC Collaboration, Acciari, V. A., Ansoldi, S., et al. 2019, *A&A*, **623**, A175
- Mannucci, F., Basile, F., Poggianti, B. M., et al. 2001, *MNRAS*, **326**, 745
- Marscher, A. P., Jorstad, S. G., D'Arcangelo, F. D., et al. 2008, *Natur*, **452**, 966
- Massaro, E., Nesci, R., Maesano, M., Montagni, F., & D'Alessio, F. 1998, *MNRAS*, **299**, 47
- Mastichiadis, A., & Moraitis, K. 2008, *A&A*, **491**, L37
- Melnikov, V. F., & Magun, A. 1998, *Solar Physics*, **178**, 153
- Miller, H. R., Carini, M. T., & Goodrich, B. D. 1989, *Natur*, **337**, 627
- Mizuno, Y., Pohl, M., Niemiec, J., et al. 2011, *ApJ*, **726**, 62
- Mizuno, Y., Pohl, M., Niemiec, J., et al. 2014, *MNRAS*, **439**, 3490
- Neshpor, Y., Chalenko, N. N., Stepanian, A. A., et al. 2001, *ARep*, **45**, 249
- Nilsson, K., Lindfors, E., Takalo, L. O., et al. 2018, *A&A*, **620**, A185
- Ojha, R., & Valverd, J. 2020, *ATel*, **13964**, 1
- Papadakis, I. E., Boumis, P., Samaritakis, V., & Papamastorakis, J. 2003, *A&A*, **397**, 565
- Papadakis, I. E., Villata, M., & Raiteri, C. M. 2007, *A&A*, **470**, 857
- Petropoulou, M., Giannios, D., & Sironi, L. 2016, *MNRAS*, **462**, 3325
- Prince, R. 2021, *MNRAS*, **507**, 5602
- Raiteri, C. M., Villata, M., Capetti, A., et al. 2009, *A&A*, **507**, 769
- Raiteri, C. M., Villata, M., Bruschini, L., et al. 2010, *A&A*, **524**, A43
- Raiteri, C. M., Villata, M., D'Ammando, F., et al. 2013, *MNRAS*, **436**, 1530
- Romero, G. E., Cellone, S. A., & Combi, J. A. 1999, *A&AS*, **135**, 477
- Sahakyan, N., & Giommi, P. 2022, *MNRAS*, **513**, 4645S
- Sasada, M., Imazawa, R., Hazama, N., & Fukazawa, Y. 2020, *ATel*, **14081**, 1
- Scarpa, R., Urry, C. M., Falomo, R., Pesce, J. E., & Treves, A. 2000, *ApJ*, **532**, 740
- Schlegel, D. J., Finkbeiner, D. P., & Davis, M. 1998, *ApJ*, **500**, 525
- Shao, C., & Huang, G. 2009, *ApJL*, **694**, L162
- Sironi, L., Petropoulou, M., & Giannios, D. 2015, *MNRAS*, **450**, 183
- Smith, P. S., Balonek, T. J., Heckert, P. A., Elston, R., & Schmidt, G. D. 1985, *AJ*, **90**, 1184
- Tammi, J., & Duffy, P. 2009, *MNRAS*, **393**, 1063
- Villata, M., Raiteri, C. M., Kurtanidze, O. M., et al. 2002, *A&A*, **390**, 407
- Villata, M., Raiteri, C. M., Aller, H. D., et al. 2004, *A&A*, **424**, 497
- Villata, M., Raiteri, C. M., Larionov, V. M., et al. 2009, *A&A*, **501**, 455
- Wagner, S. J., & Witzel, A. 1995, *ARA&A*, **33**, 163
- Weaver, Z. R., Williamson, K. E., Jorstad, S. G., et al. 2020, *ApJ*, **900**, 137
- Wierzcholska, A., Ostrowski, M., Stawarz, L., Wagner, S., & Hauser, M. 2015, *A&A*, **573**, A69
- Woo, J.-H., & Urry, C. M. 2002, *ApJ*, **579**, 530
- Zhang, Y. H., Treves, A., Celotti, A., et al. 2002, *ApJ*, **572**, 762